Evidence for unconventional superconductivity in twisted bilayer graphene

https://doi.org/10.1038/s41586-021-04121-x

Received: 16 June 2021

Accepted: 11 October 2021

Published online: 20 October 2021



Check for updates

Myungchul Oh^{1,4}, Kevin P. Nuckolls^{1,4}, Dillon Wong^{1,4}, Ryan L. Lee¹, Xiaomeng Liu¹, Kenii Watanabe², Takashi Taniquchi³ & Ali Yazdani^{1⊠}

The emergence of superconductivity and correlated insulators in magic-angle twisted bilayer graphene (MATBG) has raised the intriguing possibility that its pairing mechanism is distinct from that of conventional superconductors¹⁻⁴, as described by the Bardeen-Cooper-Schrieffer (BCS) theory. However, recent studies have shown that superconductivity persists even when Coulomb interactions are partially screened^{5,6}. This suggests that pairing in MATBG might be conventional in nature and a consequence of the large density of states of its flat bands. Here we combine tunnelling and Andreev reflection spectroscopy with a scanning tunnelling microscope to observe several key experimental signatures of unconventional superconductivity in MATBG. We show that the tunnelling spectra below the transition temperature T_c are inconsistent with those of a conventional s-wave superconductor, but rather resemble those of a nodal superconductor with an anisotropic pairing mechanism. We observe a large discrepancy between the tunnelling gap Δ_T , which far exceeds the mean-field BCS ratio (with $2\Delta_T/k_BT_c \sim 25$), and the gap Δ_{AR} extracted from Andreev reflection spectroscopy $(2\Delta_{AR}/k_BT_c \sim 6)$. The tunnelling gap persists even when superconductivity is suppressed, indicating its emergence from a pseudogap phase. Moreover, the pseudogap and superconductivity are both absent when MATBG is aligned with hexagonal boron nitride. These findings and other observations reported here provide a preponderance of evidence for a non-BCS mechanism for superconductivity in MATBG.

Tunnelling measurements of the quasiparticle density of states (DOS). the energy gap and electron-phonon coupling in conventional superconductors have provided key experimental evidence for the BCS theory of superconductivity⁷. Similar measurements on correlated superconductors, most notably using scanning tunnelling microscopy (STM) and angle-resolved photoemission spectroscopy, have shown their properties to be qualitatively different from those of BCS superconductors 8,9 . For the high- T_c cuprate superconductors, whereas tunnelling spectra in the overdoped regime can be captured by the DOS of a BCS-like model with a d-wave order parameter, the yet-to-be-understood pseudogap phenomenon at reduced doping causes the spectroscopic properties of the cuprates to strongly deviate from this picture9.

Superconductivity has been observed at remarkably low carrier densities at partial fillings of the flat bands of MATBG¹⁻³. Although these qualities suggest an unconventional pairing mechanism, conclusive evidence for any mechanism beyond the BCS paradigm is absent. We use density-tuned scanning tunnelling and point-contact spectroscopy (DT-STS and DT-PCS) to show that the superconducting phase of MATBG, specifically when hole-doping its flat valence band, shares a remarkable number of features with unconventional superconductors. Our experiments show a V-shaped gap at low temperatures and an unusual pseudogap precursor phase at higher temperatures and magnetic fields from which phase-coherent superconductivity emerges. The low-energy region of the V-shaped gap supports an anisotropic pairing mechanism with nodes in the superconducting gap function, as anticipated by some theoretical studies 10-12. The pseudogap state may signify pairing without phase coherence or a secondary phase forming above T_c and B_c . Both the pseudogap and superconductivity are absent when MATBG is commensurately aligned with the hexagonal boron nitride (hBN) substrate, suggesting that the structural characteristics and/or the C₂T symmetry of unaligned MATBG is required for stabilizing these ground states. Although we cannot rule out a phonon-based pairing mechanism^{13,14}, our results provide key constraints for an accurate theory of superconductivity in MATBG.

We performed our experiments in a home-built dilution-refrigerator STM¹⁵ instrument on devices sketched in Fig. 1a. MATBG, biased at the sample voltage V_s , rests on hBN/SiO₂/Si, while a gate voltage V_g applied to Si tunes the carrier density (see Methods). Figure 1b shows a topographic image¹⁶⁻¹⁸ of unaligned MATBG/hBN, while Fig. 1c shows DT-STS

1 loseph Henry Laboratories and Department of Physics, Princeton University, Princeton, N.L. USA, 2 Research Center for Functional Materials, National Institute for Materials, Science, Tsukuba Japan. ³International Center for Materials Nanoarchitectonics, National Institute for Materials Science, Tsukuba, Japan. ⁴These authors contributed equally: Myungchul Oh, Kevin P. Nuckolls, Dillon Wong. [™]e-mail: yazdani@princeton.edu

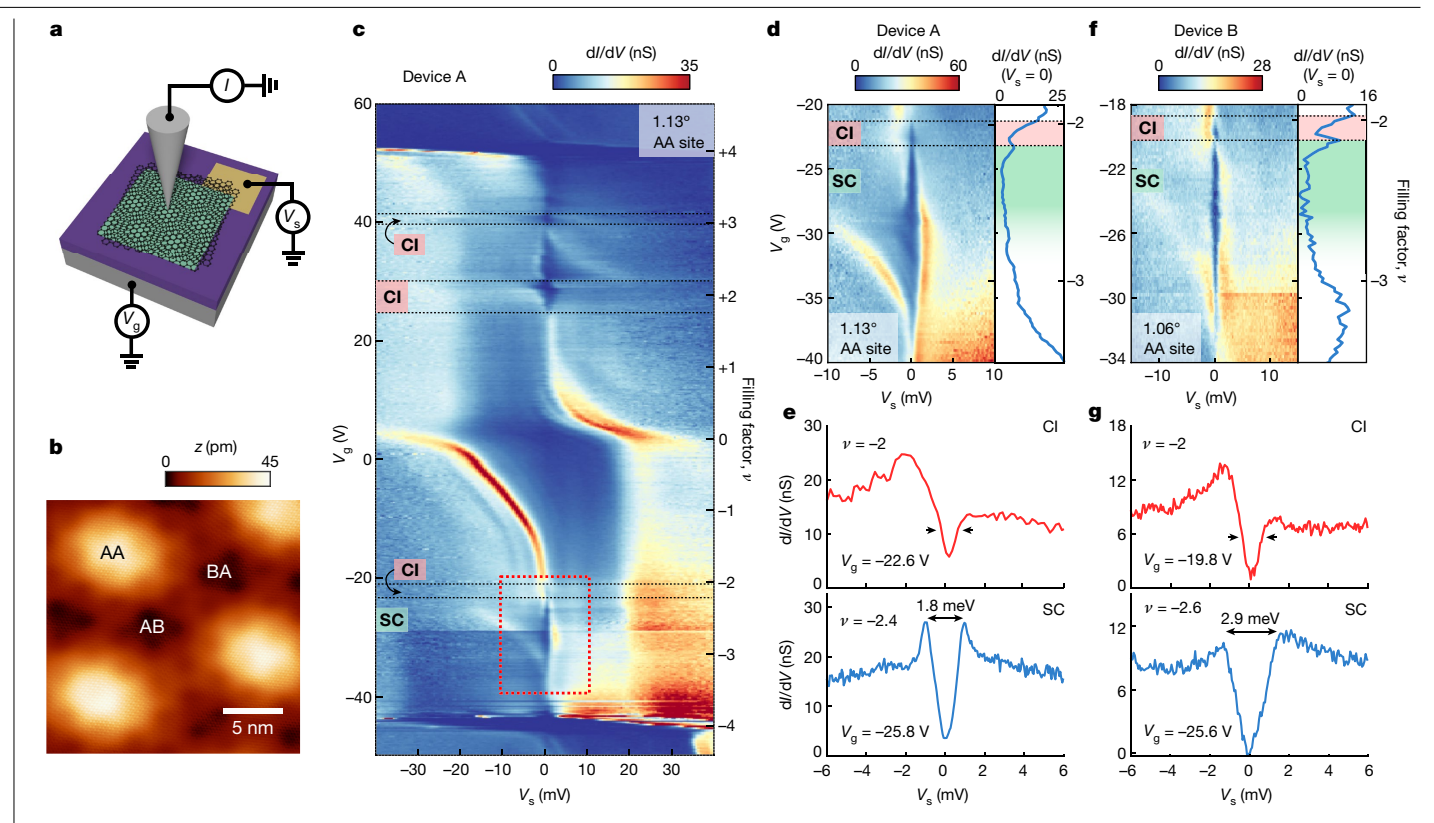


Fig. 1 | STS of the tunnelling gap of superconducting MATBG. a, The experimental set-up, showing an STM tip (from which the tunnelling current I is measured). MATBG, biased at V_s , sits atop hBN/SiO₂/Si, while V_g is applied to Si to tune the carrier density. b, STM topographic image of MATBG. c, Tunnelling $dI/dV(V_s, V_g)$ taken at the centre of an AA site in device A (1.13°, 0.4% strain) shows the conduction and valence flat bands pinned to $E_{\rm F}$. The red dashed-line box highlights a set of gaps in the valence flat band. **d**, Higher-resolution $dI/dV(V_s, V_a)$

for device A shows a gap at v = -2 (CI; correlated insulator) and a gap between v = -2 and v = -3 (SC; superconductor). A line cut of $dI/dV(V_g)$ at $V_s = 0$ V is shown on the right. **e**, $dI/dV(V_s)$ spectra for device A at $V_g = -22.6$ V (top) and $V_g = -25.8$ V (bottom). **f**, Same as **d**, except for device B (1.06°, 0.1% strain). **g**, $dI/dV(V_s)$ spectra for device B at $V_g = -19.8 \text{ V (top)}$ and $V_g = -25.6 \text{ V (bottom)}$. See Supplementary Information for tunnelling parameters.

 $dI/dV(V_s, V_g)$ acquired at 250 mK at the centre of an AA site in device A (see Supplementary Information for AB/BA data). Figure 1c shows that the conduction (valence) flat band is pinned to the Fermi energy ($E_{\rm F}$; $V_s = 0 \text{ V}$) when V_σ tunes E_F above (below) the charge neutrality point (CNP; $V_{\text{CNP}} = 3.7 \text{ V}$), while the valence (conduction) flat band onsets at $V_s < -20 \text{ mV}$ ($V_s > 20 \text{ mV}$) and displays significant energy broadening due to charge fluctuations¹⁹. At millikelyin temperatures, we observe features in DT-STS attributed to a cascade of transitions at partial band $fillings^{20-23}, but they appear weaker and broader in energy than those\\$ observed at higher temperatures (T > 4 K), which may be related to high-entropy isospin fluctuations^{24,25}.

Distinguishing nodal superconductivity

DT-STS shows several gapped phases (Fig. 1c) starting with band insulators at $v = \pm 4$, where v is the electron filling per moiré unit cell relative to the CNP. Here we focus on partial fillings of the valence flat band near $-3 < \nu < -2$, where transport studies¹⁻³ report superconductivity in MATBG (Fig. 1c, red box). Figure 1d, f shows tunnelling spectra dI/ $dV(V_s, V_g)$ from two devices (device A as in Fig. 1c and device B), which display a gap at v = -2 that opens and closes at E_F with decreasing V_g , followed by the opening of a new gap that persists in the range -3 < v < -2. The density dependence of these gaps is highlighted by $dI/dV(V_s = 0 \text{ V})$ as a function of V_g shown in Fig. 1d, f. We observe a clear transition between the two gapped phases, consistent with the phase diagram of MATBG from transport studies 1-3,5,6 in which a correlated insulator at v = -2 transitions into a superconductor that persists for -3 < v < -2. In Fig. 1e, g, we plot tunnelling gaps for the v = -2 correlated

insulator (red curves) and the -3 < v < -2 superconductor (blue curves) measured in each device. The -3 < v < -2 tunnelling gap is significantly larger than $k_B T_c$ observed in transport experiments¹⁻³ and is an order of magnitude larger than an in-plane tunnelling gap observed in a MATBG p-n junction²⁶ (presumably, the lateral p-n junction probes only the edge of the superconducting dome adjacent to the correlated insulator, instead of optimal doping, due to the junction's doping gradient). Before examining the shapes of the tunnelling spectra further, we discuss our method for distinguishing between gapped insulating and superconducting phases by complementing DT-STS with PCS measurements.

As both correlated insulators and superconductors show suppressions in $dI/dV(V_s = 0 \text{ V})$, we require complementary information that distinguishes these two phases. We performed PCS by reducing the tip height above the sample until the tip makes point contact with the sample surface (sketched in Fig. 2a) and then measuring the two-terminal tip-sample conductance $G(V_s, V_g)$ (see Methods; see Supplementary Information for discussion of possible tip-induced pressure and strain during PCS). This measurement is particularly sensitive to the local region beneath the tip (see Supplementary Information). The PCS zero-bias conductance $G(V_s = 0 \text{ V}, V_g)$, plotted in Fig. 2b (device A'-a different region of device A) as a function of V_g , vanishes at $v = \pm 4$ and $v = \pm 2$, signalling the formation of band and correlated insulators (Fig. 2b; red shaded bars). Consistent with transport studies¹⁻³, the insulating states are insensitive to application of a weak out-ofplane magnetic field B. In contrast, the PCS zero-bias conductance displays enhanced intensity in the range -3 < v < -2 (Fig. 2b; green shaded bar) that is suppressed with increasing B, consistent with

Article

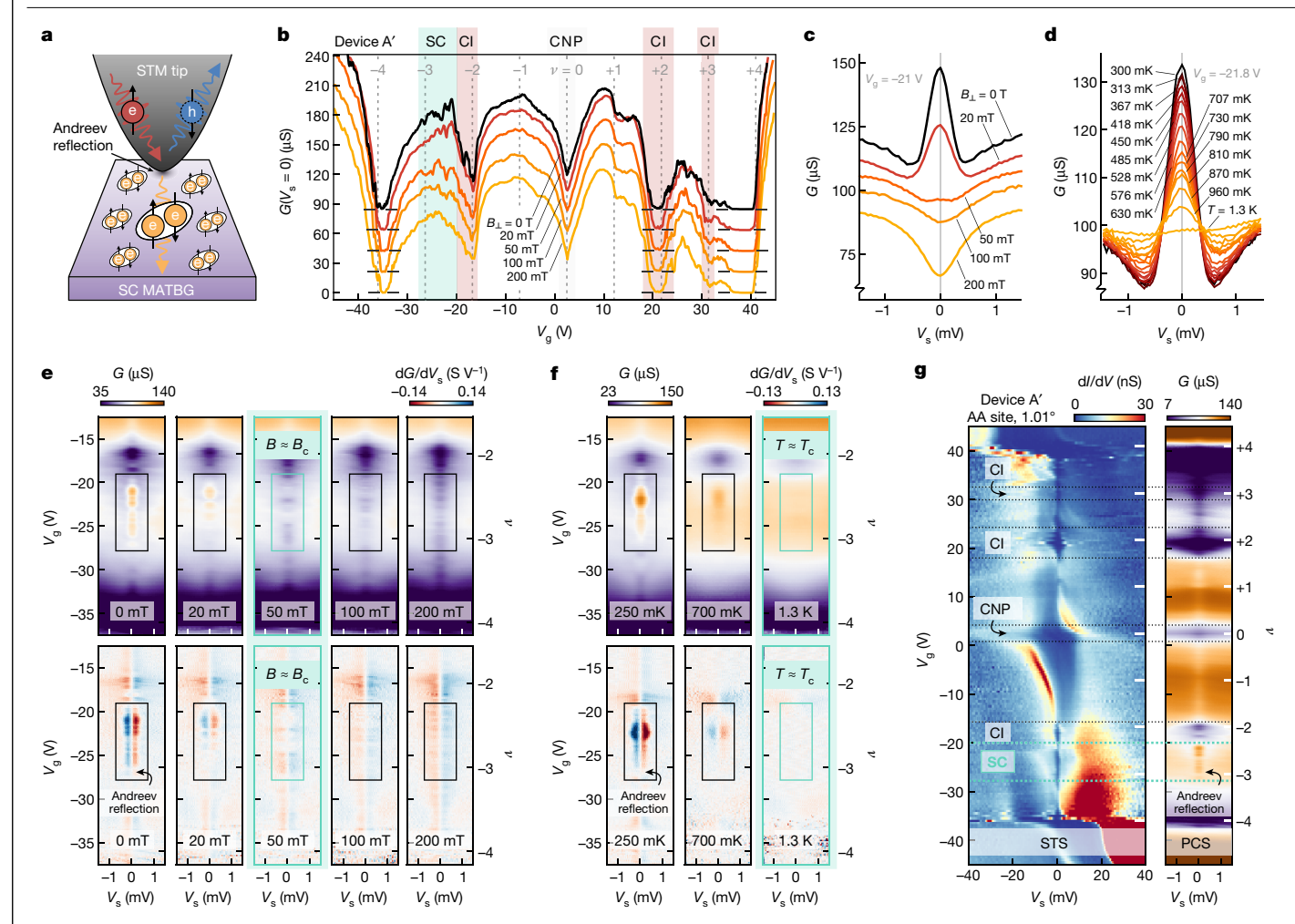


Fig. 2 | PCS and Andreev reflection for MATBG. a. The Andreev reflection process measured using DT-PCS. The STM tip is brought into point contact with the surface of MATBG, and the two-terminal conductance $G(V_s, V_g)$ is measured. **b**, Line cut of point-contact $G(V_g)$ at $V_s = 0$ V for device A' (same as device A, different region: 1.01° twist angle, 0.2% strain) at five magnetic field strengths between 0 T and 200 mT. Strong suppressions of $G(V_a)$ occur near v = -2, +2 and +3 as a result of correlated insulating phases near these integer fillings (CI; red shaded bars). A dip in $G(V_g)$ occurs near charge neutrality (CNP; grey shaded bar). An enhancement of $G(V_g)$ occurs between v = -2 and v = -3 as a result of the excess current measured in the superconducting phase (SC; green shaded bar). Curves are vertically offset by the horizontal black lines for clarity. c, Line cut of point-contact $G(V_s)$ spectra at $V_g = -21 \text{ V}$, in the superconducting carrier-density

range, at five magnetic-field strengths between 0 T and 200 mT. Curves are offset for clarity. **d**, Line cut of point-contact $G(V_s)$ spectra at $V_g = -21.8$ V, in the $superconducting\ carrier-density\ range, at\ 16\ temperatures\ between\ 300\ mK$ and 1.3 K. **e**, Point-contact $G(V_s, V_g)$ and $dG/dV_s(V_s, V_g)$ for different values of the out-of-plane magnetic field showing the disappearance of Andreev reflection at around 50 mT. f, Point-contact $G(V_s, V_g)$ and $dG/dV_s(V_s, V_g)$ for different values of the temperature showing the disappearance of Andreev reflection at around 1.3 K.g, Side-by-side tunnelling $dI/dV(V_s, V_g)$ into an AA site and point-contact $G(V_s, V_g)$ in the same location in device A'. Gaps observed in tunnelling marked as CI coincide with highly resistive states in $G(V_s, V_g)$, while the tunnelling gap marked as SC coincides with Andreev reflection. See the Supplementary Information for tunnelling and PCS parameters.

superconductivity in this doping range. More direct evidence for superconductivity is revealed by the voltage-bias dependence of PCS $G(V_s, V_g)$ in Fig. 2c, d. These spectra are indicative of Andreev reflection^{27,28}, where incoming electrons from the metallic tip are reflected as holes while Cooper pairs propagate into the superconducting sample (Fig. 2a). This results in enhanced conductance at low biases and 'excess current' when the sample is superconducting. Signatures of Andreev reflection in PCS $G(V_s, V_g)$ (black boxes in Fig. 2e, f) are limited roughly to fillings -3 < v < -2, magnetic fields $B < B_c \sim 50$ mT and temperatures $T < T_c \sim 1.2$ K, all of which are consistent with transport measurements¹⁻³. A side-by-side comparison of STS and PCS (Fig. 2g) at the same sample location shows how PCS can clearly distinguish tunnelling gaps associated with superconductivity from those associated with insulators. Despite the presence of many correlation-driven gaps at $E_{\rm F}$ in STS, only the filling range -3 < v < -2 shows both a V-shaped gap in STS and a zero-bias conductance peak in PCS.

Two distinct energy scales and the pseudogap

Both STS and PCS provide complementary evidence for an anisotropic pairing mechanism of superconductivity in MATBG. Moreover, these measurements establish two distinct energy scales. Low-energy STS spectra (Fig. 3a) are clearly incompatible with an isotropic s-wave pairing symmetry, and the best fits to such a model require introducing unphysically large quasiparticle broadening (equivalent to an electron temperature above 2 K; for comparison, see Supplementary Informa $tion for STS \, on \, superconducting \, Al). \, Often \, STS \, spectra \, on \, MATBG \, have \, determined a continuous contin$ a finite conductance at zero energy, but V-shaped spectra with zero conductance at zero bias have also been observed (Fig. 1g). These STS spectra resemble the quasiparticle DOS of a nodal superconductor, as for higher-angular-momentum (for example, p- or d-wave) pairing with an anisotropic gap function (Fig. 3b shows this fit for device A, $V_g = -25.8 \text{ V}$ —see the Supplementary Information for fits at other V_g).

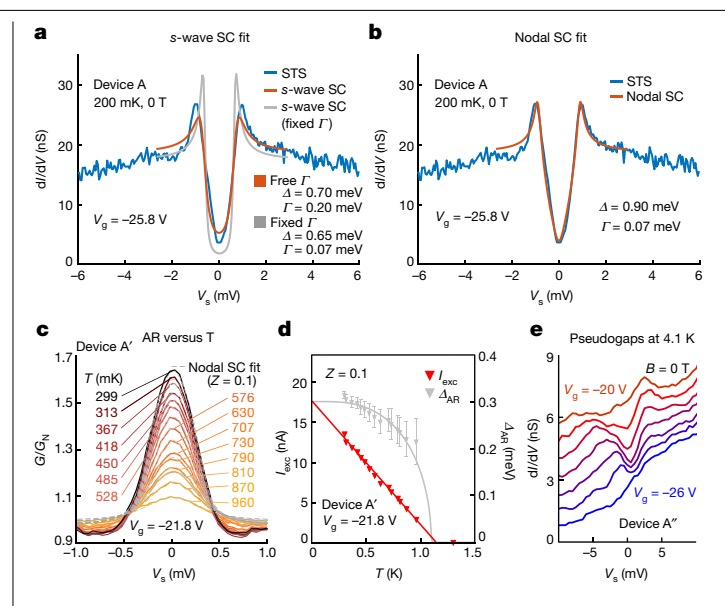
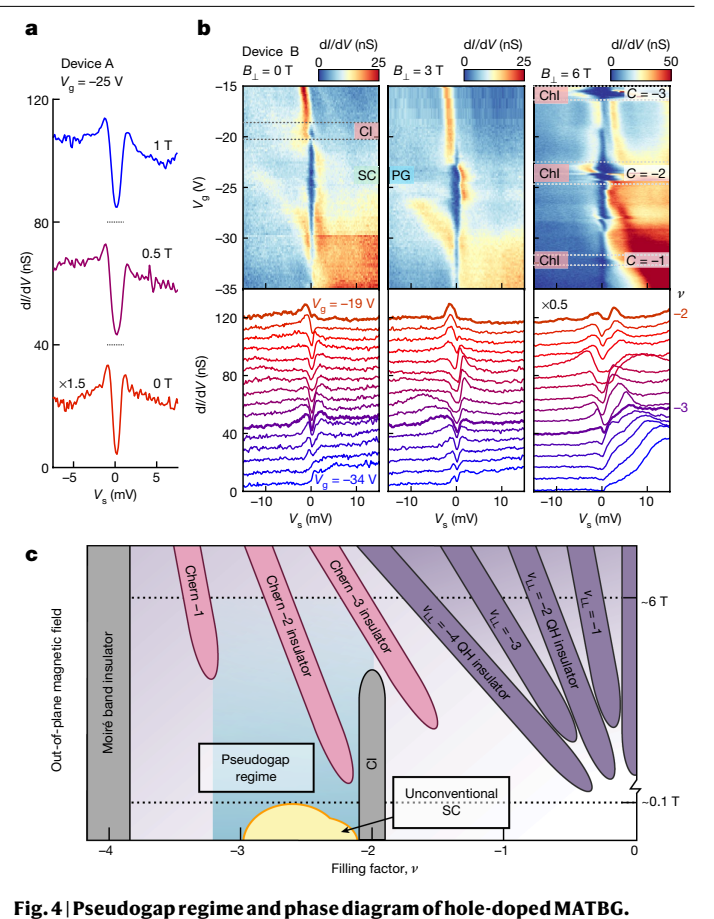


Fig. 3 | Tunnelling and Andreev reflection spectra curve fits. a,

Dynes-function fits to the experimental tunnelling spectrum (blue curve) measured at $V_{\sigma} = -25.8 \text{ V}$ for device A at 200 mK and B = 0 T using the model quasiparticle DOS for a nodeless s-wave superconductor with all free parameters (red curve) and with fixed lifetime broadening parameter $\Gamma = 0.07$ meV (grey curve) (see Supplementary Information for details). b, Same as a, except using the model quasiparticle DOS for a nodal superconductor (for example, p-, d- and f-wave). c, Normalized Andreev reflection spectra (solid curves, normalized with the normal state conductance G_N) obtained in device A' at $V_{\sigma} = -21.8 \text{ V}$ at 15 temperatures between 300 mK and 1 K, fitted with the BTK model (dotted curves) with fixed barrier transparency parameter Z = 0.1. **d**, Excess current I_{exc} and the superconducting energy gap Δ_{AR} extracted from the BTK fits in \mathbf{c} (see Supplementary Information for details). The error bars represent the standard deviation of the fitted energy gap. The excess current shows an anomalous linear dependence on the temperature, indicative of unconventional superconductivity. **e**, Tunnelling $dI/dV(V_s)$ spectra acquired at the centre of an AA site between $V_{\rm g}$ = -20 V and $V_{\rm g}$ = -26 V in device A" (same as device A, different region; 0.99° twist angle), measured at T = 4.1 K. Curves are offset by 0.6 nS for clarity. A suppression of the DOS near $E_{\rm F}$ is observed at temperatures above $T_{\rm c}$ for superconductivity observed at -3 < v < -2 (see Supplementary Information for full $dI/dV(V_s, V_g)$ for all observations of the high-temperature pseudogap phase). See Supplementary Information for tunnelling parameters.

Although the nodal fit describes this spectrum well, one should be cautious about this interpretation given the similar appearance of this gap to that of the pseudogap above T_c and B_c described below. Nevertheless, we extract an energy scale of $\Delta_T \sim 0.9$ meV from this fit, which roughly corresponds to half the separation of the shoulders in the spectrum. Similarly, the Andreev reflection spectra in PCS resemble predictions from the Blonder-Tinkham-Klapwijk (BTK) model²⁹ using a nodal superconducting gap function (Fig. 3c and Supplementary Information). However, a BTK-model fit yields an energy scale Δ_{AR} ~ 0.3 meV (device A': V_g = -22.8 V), 3-5 times smaller than Δ_T . For $T_c \approx 1.2 \text{ K}$ (measured through PCS), the observed ratio $2\Delta_T/k_B T_c \sim 25$ (device A'; $V_g = -22.8 \text{ V}$) is significantly higher than the expected ratio for a tunnelling gap of a BCS superconductor ($2\Delta_{MF}/k_BT_c = 3.53$). The Andreev energy-scale ratio $2\Delta_{AR}/k_{B}T_{c}$ ~ 6 also appears to be higher than the BCS ratio. As noted above, Andreev reflection disappears when phase-coherent superconductivity is absent, with both Δ_{AR} and the Andreev excess current vanishing above T_c and B_c (Figs. 2d and 3d). In contrast, the STS gap Δ_T persists when phase-coherent superconductivity vanishes above T_c (see Fig. 3e and Supplementary Information) and well above B_c (Fig. 4).

A similar dichotomy between the energy scales describing tunnelling and Andreev reflection has been documented for the underdoped



a, Tunnelling $dI/dV(V_s)$ spectra at $V_g = -25$ V taken at the centre of an AA site in device A at B_{\perp} = 0 T (red curve), 0.5 T (purple curve) and 1 T (blue curve), which show the persistence of a prominent gap at $E_{\rm F}$ well above $B_{\rm c}$ for MATBG. **b**, Tunnelling $dI/dV(V_s, V_g)$ and $dI/dV(V_s)$ spectra on an AA site in device B for $V_{\sigma} = -19 \text{ V to } V_{\sigma} = -34 \text{ V and for } B_{\perp} = 0 \text{ T}, 3 \text{ T and } 6 \text{ T}. \text{ Curves are offset by 7.5 nS for}$ clarity. At $B_{\perp} = 0$ T, a gap opens and closes near v = -2 due to the correlated insulating (CI) phase, followed by a gap for the superconducting phase at -3 < v < -2. At $B_{\perp} = 3$ T; the gap at -3 < v < -2 is a result of the pseudogap (PG) regime. At B_{\perp} = 6 T, a series of large gaps appear that correspond to correlated Chern insulating (ChI) phases with Chern numbers C = -3, -2, -1. See Supplementary Information for tunnelling parameters. c, A proposed phase diagram for MATBG as a function of flat-band filling factor v and magnetic field B_{\perp} in the hole-doped regime. (v_{LL} is the Landau-level filling factor.) Near -3 < v < -2, we observe an unconventional superconducting phase at low magnetic fields, which transitions into a pervasive pseudogap regime at high

magnetic fields. QH, quantum Hall.

cuprate superconductors²⁷, where Andreev reflection also tracks the onset of phase coherence at T_c while the tunnelling gap persists above T_{c} , as we observe in MATBG (see high-temperature data in the Supplementary Information; see also ref. ²³). Compared to studies^{8,9} that examine the relationship between the pseudogap and superconductivity in the cuprates, in MATBG, we have the advantage that application of a relatively weak $B > B_c \sim 50$ mT suppresses phase coherence at low temperatures, allowing us to probe the shape of the pseudogap spectra with high energy resolution at the lowest temperatures. Such meas $urements in Fig.\,4a \, show \, that \, the \, shapes \, of \, the \, spectra \, in \, the \, pseudogap$ phase remain remarkably sharp and surprisingly similar to those of spectra observed when the sample is superconducting. While the v = -2correlated insulator is suppressed below 3 T, the pseudogap remains present over most of the doping range -3 < v < -2 (Fig. 4b). The density dependence of the STS at zero magnetic field and up to 3 T (see the Supplementary Information for 1 T data) reveals that the onset of a

Article

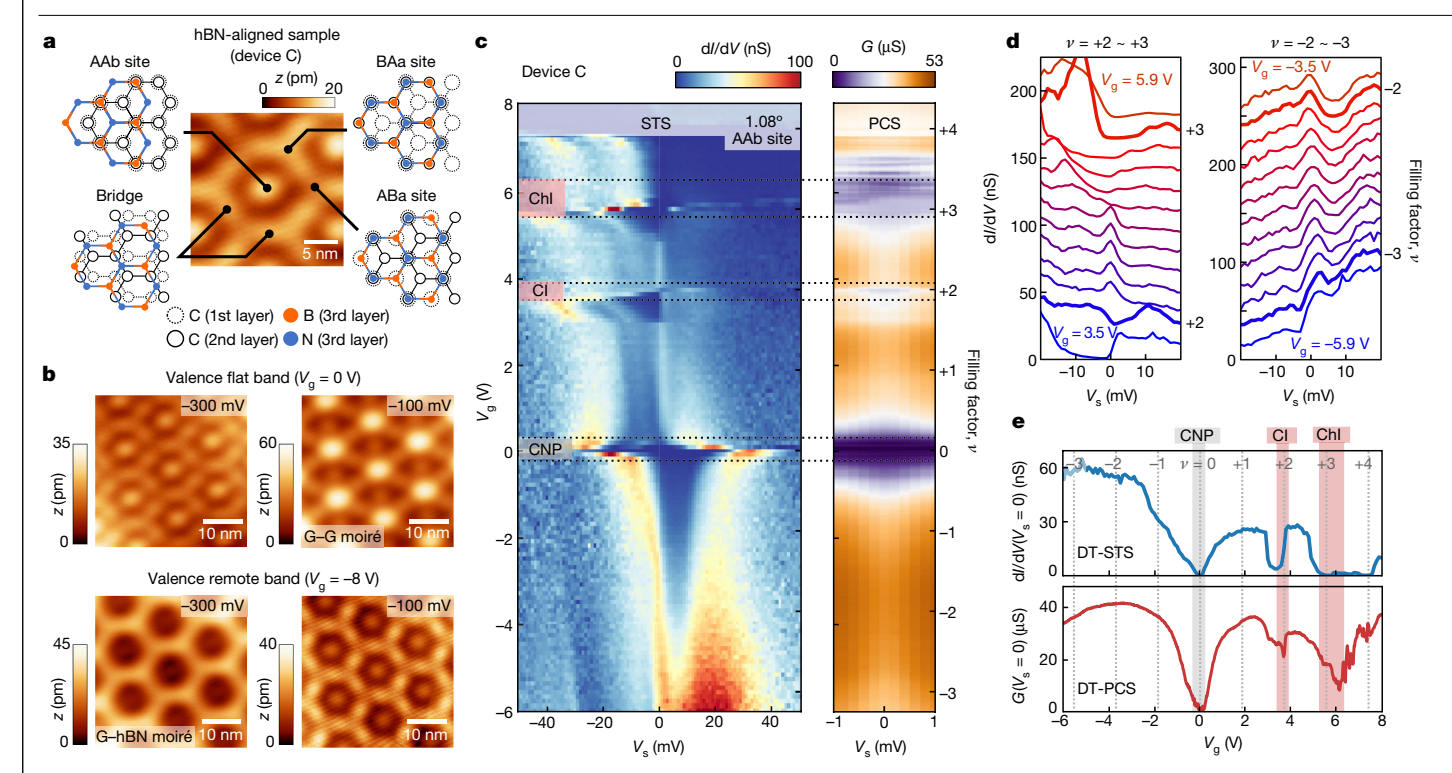


Fig. 5 | **DT-STS and DT-PCS on non-superconducting MATBG aligned to hBN. a**, STM topographic image of MATBG that is perfectly commensurate with the underlying hBN substrate. Atomistic schematics show the stacking configurations of carbon, boron and nitrogen for different regions of the moiré pattern. **b**, STM topographic images of MATBG aligned to hBN for different values of V_s and V_g , highlighting the graphene (G–G) moiré pattern and the graphene–hBN (G–hBN) moiré pattern. **c**, Side-by-side comparison of tunnelling

 $dl/dV(V_s,V_g)$ into an AAb site and point-contact $G(V_s,V_g)$ for device C (1.08° G–G twist angle, 0.1% G–G interlayer strain, 0.5 \pm 0.1° G–hBN twist angle), which uses a graphite gate instead of a silicon gate. No signatures of a superconducting gap or a pseudogap or of Andreev reflection can be seen in either measurement. \mathbf{d} , $dl/dV(V_s)$ spectra from \mathbf{c} , offset by 15 nS (left) and 20 nS (right) for clarity. \mathbf{e} , Tunnelling $dl/dV(V_g)$ and PCS $G(V_g)$ line cuts from \mathbf{c} for $V_s = 0$ V.

See Supplementary Information for tunnelling and spectroscopy parameters.

sharp pseudogap in the absence of phase-coherent superconductivity occurs when the van Hove singularity associated with the valence band overlaps with $E_{\rm F}$. In this situation, the gain in the exchange energy may favour the formation of an isospin (spin/valley)-polarized/coherent ground state (or some other ordered state), which may be responsible for the pseudogap with sharp side peaks shown in Fig. 4a. However, given the remarkable resemblance between the shapes of the STS gaps in the pseudogap and superconducting phases, it is also possible that such a gap is driven by the formation of incoherent pairs for $B > B_c$ and $T > T_c$ (ref. 30). Regardless of the origin, the correlations responsible for the pseudogap are clearly compatible with the onset of phase-coherent superconductivity.

Quenching pairing and pseudogap with hBN

Further insight into superconductivity and the pseudogap phase in MATBG is provided by studying MATBG aligned with hBN. Anecdotally, transport experiments do not report superconductivity in MATBG samples that are presumed to be well aligned with hBN (refs. 31,32). In examining the role of hBN alignment, STM studies are particularly advantageous, as they can directly visualize and distinguish the graphene–graphene (G–G) and graphene–hBN (G–hBN) moiré structures. Figure 5b shows a set of representative topographic images of device C, taken at different $V_{\rm s}$ and $V_{\rm g}$ to disentangle the different structural roles of the two moiré patterns (see Supplementary Information). Surprisingly, these images show perfect alignment between the AA sites of the G–G moiré and the carbon–boron regions of the G–BN moiré. This suggests a propensity for MATBG aligned to hBN to undergo a moiré-scale incommensurate–commensurate transition when the two moiré length scales are similar. In the schematic in Fig. 5a, we label

these substrate-modified AA sites as AAb sites to reflect this alignment configuration. Likewise, the AB/BA sites of MATBG are made inequivalent by the hBN, forming ABa (BAa) regions where atoms in the top (bottom) graphene sheet are in register with atoms in the top hBN layer. This incommensurate—commensurate transition contrasts with the formation of a super-superlattice due to a long-wavelength interference between the two moiré patterns.

DT-STS and DT-PCS on device C show that alignment with hBN dramatically alters the electronic properties of MATBG (Fig. 5c-e). In contrast to the semi-metallic behaviour we observe in unaligned samples at the CNP, the STS spectrum acquired at the centre of an AAb site shows a gap (convolved with Coulomb charging effects) at the Dirac point due to sublattice symmetry breaking 33-35, and the resulting insulating behaviour of MATBG at the CNP is directly probed using PCS (Fig. 5c, e). In agreement with transport studies 31,32, our study finds correlated and Chern insulators at v = +2 and +3, respectively (Fig. 5c; see also Supplementary Information). In contrast with unaligned samples, aligned samples show neither a cascade of transitions nor evidence for superconductivity or the pseudogap, despite the twist angle of this device (1.08°) being near those with the maximal T_c in transport measurements on unaligned devices^{1,5}. Overall, DT-STS and DT-PCS show that hBN alignment is detrimental to the formation of both the pseudogap and the superconducting phases of MATBG, as evidenced by contrasting data in Figs. 1 and 2 with those of Fig. 5. Furthermore, the ability to identify superconductivity and a pseudogap phase in unaligned MATBG and their absence in MATBG aligned to hBN demonstrates the utility of our combined DT-STS and DT-PCS technique, as the existence of superconductivity in some flat-band materials 36 as well as the importance of C_2T symmetry $^{37-39}$ is currently heavily contested.

Discussion

Cumulatively, our findings provide substantial evidence that pairing in MATBG is unconventional and distinct from that of a BCS mechanism. STS does not show an isotropic gap with a size consistent with that expected from a T_c ~ 1.2 K s-wave BCS superconductor, but shows a V-shaped DOS consistent with that of a nodal superconductor, where the details of the spectra vary with twist angle and strain (see Supplementary Information). The PCS measurements corroborate this picture and additionally show an unusual linear suppression of the Andreev excess current approaching T_c (Fig. 3d). This behaviour is $similar \ to \ that \ reported \ in \ other \ unconventional \ superconductors^{40,41}$ and has been suggested to be related to pair-breaking effects due to inelastic scattering from bosonic modes. There are many candidates for bosonic modes in MATBG, ranging from phonons to more exotic collective isospin fluctuations⁴²; however, a key ingredient for this scenario is the presence of a sign-changing order parameter, which makes scattering from such modes pair breaking⁴³. As an aside, if pairing is spin-triplet in nature, the ratio of the enhanced conductance near zero bias to the background conductance in the Andreev spectra is incompatible with an equal-spin-pairing order parameter (see Supplementary Information). Moreover, like the underdoped cuprate superconductors²⁷, MATBG shows contrasting behaviour between the energy scales describing tunnelling and Andreev reflection. Without further experiments, it is difficult to distinguish between different explanations for this dichotomy (that is, a precursor broken-symmetry phase or preformed pairing without coherence³⁰). Overall, the experiments presented here provide clear constraints for constructing a model of the pairing mechanism in this novel electronic material that lies beyond the BCS paradigm.

Online content

Any methods, additional references, Nature Research reporting summaries, source data, extended data, supplementary information, acknowledgements, peer review information; details of author contributions and competing interests; and statements of data and code availability are available at https://doi.org/10.1038/s41586-021-04121-x.

- Cao, Y, et al. Unconventional superconductivity in magic-angle graphene superlattices. 1. Nature 556, 43-50 (2018)
- 2. Yankowitz, M. et al. Tuning superconductivity in twisted bilayer graphene. Science 363 1059-1064 (2019).
- 3. Lu. X. et al. Superconductors, orbital magnets and correlated states in magic-angle bilayer graphene. Nature 574, 653-657 (2019).
- Cao, Y. et al. Correlated insulator behaviour at half-filling in magic-angle graphene superlattices. Nature 556, 80-84 (2018).
- 5. Saito, Y., Ge, J., Watanabe, K., Taniguchi, T. & Young, A. F. Independent superconductors and correlated insulators in twisted bilayer graphene. Nat. Phys. 16, 926-930 (2020).
- Stepanov, P. et al. Untying the insulating and superconducting orders in magic-angle graphene. Nature **583**, 375-378 (2020).
- 7. Bardeen, J. Electron-phonon interactions and superconductivity. Science 181, 1209-1214
- Damascelli, A., Hussain, Z. & Shen, Z.-X. Angle-resolved photoemission studies of the cuprate superconductors. Rev. Mod. Phys. 75, 473-541 (2003).
- Fischer, Ø., Kugler, M., Maggio-Aprile, I., Berthod, C. & Renner, C. Scanning tunneling spectroscopy of high-temperature superconductors. Rev. Mod. Phys. 79, 353-419 (2007).
- Isobe, H., Yuan, N. F. Q. & Fu, L. Unconventional superconductivity and density waves in twisted bilayer graphene. Phys. Rev. X 8, 041041 (2018).
- Liu, C.-C., Zhang, L.-D., Chen, W.-Q. & Yang, F. Chiral spin density wave and d+id superconductivity in the magic-angle-twisted bilayer graphene. Phys. Rev. Lett. 121, 217001 (2018).

- Kennes, D. M., Lischner, J. & Karrasch, C. Strong correlations and d+id superconductivity in twisted bilayer graphene. Phys. Rev. B 98, 241407 (2018).
- Wu, F., MacDonald, A. H. & Martin, I. Theory of phonon-mediated superconductivity in twisted bilayer graphene. Phys. Rev. Lett. 121, 257001 (2018).
- Lian, B., Wang, Z. & Bernevig, B. A. Twisted bilayer graphene: a phonon-driven superconductor. Phys. Rev. Lett. 122, 257002 (2019).
- Wong, D. et al. A modular ultra-high vacuum millikelvin scanning tunneling microscope Rev. Sci. Instrum. 91, 023703 (2020).
- Kerelsky, A. et al. Maximized electron interactions at the magic angle in twisted bilayer graphene, Nature 572, 95-100 (2019).
- Choi, Y. et al. Electronic correlations in twisted bilayer graphene near the magic angle. Nat Phys 15 1174-1180 (2019)
- Jiang, Y. et al. Charge order and broken rotational symmetry in magic-angle twisted bilayer graphene. Nature 573, 91-95 (2019).
- Xie, Y. et al. Spectroscopic signatures of many-body correlations in magic-angle twisted bilayer graphene. Nature 572, 101-105 (2019).
- 20. Wong, D. et al. Cascade of electronic transitions in magic-angle twisted bilayer graphene. Nature 582, 198-202 (2020).
- Zondiner, U. et al. Cascade of phase transitions and Dirac revivals in magic-angle graphene, Nature 582, 203-208 (2020).
- Nuckolls. K. P. et al. Strongly correlated Chern insulators in magic-angle twisted bilayer graphene, Nature 588, 610-615 (2020).
- Choi. Y. et al. Interaction-driven band flattening and correlated phases in twisted bilayer graphene. Nat. Phys. https://doi.org/10.1038/s41567-021-01359-0 (2021).
- 24. Saito, Y. et al. Isospin Pomeranchuk effect in twisted bilayer graphene. Nature 592, 220-224 (2021).
- Rozen, A. et al. Entropic evidence for a Pomeranchuk effect in magic-angle graphene. Nature 592, 214-219 (2021).
- 26. Rodan-Legrain, D. et al. Highly tunable junctions and non-local Josephson effect in magic-angle graphene tunnelling devices. Nat. Nanotechnol. 16, 769-775 16, 769-775
- Deutscher, G. Andreev-Saint-James reflections: a probe of cuprate superconductors. Rev. Mod. Phys. 77, 109-135 (2005).
- Dubouchet, T. et al. Collective energy gap of preformed Cooper pairs in disordered superconductors. Nat. Phys. 15, 233-236 (2019).
- Blonder, G. E., Tinkham, M. & Klapwijk, T. M. Transition from metallic to tunneling regimes in superconducting microconstrictions: excess current, charge imbalance, and supercurrent conversion. Phys. Rev. B 25, 4515-4532 (1982).
- Randeria, M., Trivedi, N., Moreo, A. & Scalettar, R. T. Pairing and spin gap in the normal state of short coherence length superconductors, Phys. Rev. Lett. 69, 2001-2004 (1992).
- 31. Serlin, M. et al. Intrinsic quantized anomalous Hall effect in a moiré heterostructure. Science 367, 900-903 (2020).
- Sharpe, A. L. et al. Emergent ferromagnetism near three-quarters filling in twisted bilayer graphene, Science 365, 605-608 (2019).
- Hunt, B. et al. Massive Dirac fermions and Hofstadter butterfly in a van der Waals heterostructure, Science 340, 1427-1430 (2013).
- Shi, J., Zhu, J. & MacDonald, A. H. Moiré commensurability and the quantum anomalous Hall effect in twisted bilayer graphene on hexagonal boron nitride. Phys. Rev. B 103, 075122 (2021).
- Zhang, Y.-H., Mao, D. & Senthil, T. Twisted bilayer graphene aligned with hexagonal boron nitride: anomalous Hall effect and a lattice model. Phys. Rev. Res. 1, 033126 (2019).
- 36. He, M. et al. Symmetry breaking in twisted double bilayer graphene. Nat. Phys. 17, 26-30 (2021).
- Khalaf, E., Chatterjee, S., Bultinck, N., Zaletel, M. P. & Vishwanath, A. Charged skyrmions 37. and topological origin of superconductivity in magic-angle graphene. Sci. Adv. 7, eabf5299 (2021).
- Park, J. M., Cao, Y., Watanabe, K., Taniguchi, T. & Jarillo-Herrero, P. Tunable strongly coupled superconductivity in magic-angle twisted trilayer graphene. Nature 590, 249-255 (2021).
- Hao, Z. et al. Electric field-tunable superconductivity in alternating-twist magic-angle trilayer graphene. Science 371, 1133-1138 (2021).
- Goll, G., Löhneysen, H. V., Yanson, I. K. & Taillefer, L. Anisotropy of point-contact spectra in the heavy-fermion superconductor UPt₂, Phys. Rev. Lett. 70, 2008-2011 (1993).
- Laube, F., Goll, G., Eschrig, M., Fogelström, M. & Werner, R. Excess current in superconducting Sr₂RuO₄, Phys. Rev. B 69, 014516 (2004).
- Khalaf, E., Bultinck, N., Vishwanath, A. & Zaletel, M. P. Soft modes in magic angle twisted 42. bilayer graphene. Preprint at https://arxiv.org/abs/2009.14827v2 (2020).
- Millis, A. J., Sachdev, S. & Varma, C. M. Inelastic scattering and pair breaking in anisotropic and isotropic superconductors. Phys. Rev. B 37, 4975-4986 (1988).

Publisher's note Springer Nature remains neutral with regard to jurisdictional claims in published maps and institutional affiliations.

© The Author(s), under exclusive licence to Springer Nature Limited 2021

Article

Methods

STM measurements

STM/STS measurements were performed on a home-built dilution-refrigerator STM 15 with tungsten tips prepared on a Cu(111) surface. The carrier density in MATBG was tuned by a gate voltage $V_{\rm g}$ applied to Si (or a graphite gate for device C), while $V_{\rm s}$ was applied to the sample. dI/dV was measured through lock-in detection of the a.c. tunnel current in response to an a.c. modulation $V_{\rm rms}$ added to $V_{\rm s}$. Initial tunnelling parameters for STS were chosen to avoid phonon-induced inelastic tunnelling 44 .

We used two experimental protocols for avoiding unwanted local gating from the tip²⁰. First, we used an STM tip that had been freshly prepared (field emission, pulsing, poking) and calibrated on a cleaned single-crystal metal, paying particular attention to protecting the tip from polymer residue contamination that often lies on the surface of two-dimensional material devices. Second, we used an STM tip and metal crystal made of materials (for example, tungsten and copper) that are workfunction-matched with graphene. Careful preparation of the tip and sample are essential because when polymer residue on the device's surface attaches to the tip, spectroscopic features of the tunnel junction are compromised, and topographic images often show 'drag patterns' caused by the motion of a particle in the tunnel junction or by flexing of the tip apex⁴⁵⁻⁴⁷. As these drag patterns may be misinterpreted as tip-induced strain effects, we provide evidence of our clean and stable tip-sample junctions in Supplementary Fig. 16, which shows two topographic images without a drag pattern that are essentially identical despite a three-orders-of-magnitude change in the junction resistance.

PCS measurements

PCS measurements were performed by moving the STM tip a few nanometres (relative to the tip height during tunnelling) into the MATBG surface. This does not damage the graphene. Differential conductance $G(V_s, V_g)$ was then measured through lock-in detection of the a.c. current in response to an a.c. modulation $V_{\rm rms}$ added to V_s , while ${\rm d}G/{\rm d}V_s(V_s, V_g)$ is simply the numerical derivative of the measured $G(V_s, V_g)$. We note that the conductance $G(V_s)$ appears to be slightly suppressed around zero bias in the metallic state of MATBG at millikelvin temperatures, but this suppression vanishes at T=1.3 K. As this suppression is present at all V_g and at magnetic fields above B_c , we conjecture that this is due to non-Ohmic contact, possibly between the graphene and the Ti/Au electrodes. When MATBG is superconducting, the finiteness of the critical current and the proximity effect may also contribute to the suppression of the conductance around the Andreev peaks⁴⁸. See the Supplementary Information for more details on the PCS measurements.

The data in Fig. 2b, c, e, f were acquired together, and the data in Fig. 2d, g were acquired together. Between these two sets of data, the tip was withdrawn from the surface, and then point contact was re-established in the same location. The temperature-dependent data in Fig. 2d were acquired by heating the 3 He- 4 He mixture to T=1.3 K and then measuring PCS as the dilution refrigerator was cooled. The temperatures in Fig. 2d were measured via a RuO₂ thermometer in the STM head. The tip probably drifts relative to the sample during this measurement.

As Yankowitz et al. 2 have shown that superconductivity in twisted bilayer graphene can be tuned with pressure, we examined the role of tip-induced pressure/strain during a PCS measurement. Supplementary Fig. 6 shows tip-height-dependent PCS, showing that the energy scale for Andreev reflection Δ_{AR} is unchanged as the tip is pressed further into MATBG. This, along with the fact that the density range, T_c and

 $B_{\rm c}$ of superconductivity in PCS match those of transport experiments, verifies the one-to-one correspondence of STS and PCS at the same location. See Supplementary Section D for further discussion.

Sample preparation

Devices were fabricated using a 'tear-and-stack' method⁴⁹ in which a single graphene sheet is torn in half by van der Waals interaction with hBN. The two halves are rotated relative to each other and stacked to form MATBG. As device B is device A from ref. 20, a full description of the fabrication procedure can be found therein. To summarize, graphene and hBN are picked up with polyvinyl alcohol. Then, to flip the heterostructure upside down, the heterostructure is pressed against an intermediate structure consisting of polymethyl methacrylate/ transparent tape/Sylgard 184, and the polyvinyl alcohol is dissolved via water injection. The heterostructure is then transferred to a SiO₂/Si chip with pre-patterned Ti/Au electrodes. Residual polymer is dissolved in dichloromethane, water, acetone and isopropyl alcohol. This chip is annealed in ultrahigh vacuum at 170 °C overnight and 400 °C for 2 h. Device A is prepared in a similar manner, except the polymethyl methacrylate is replaced with Elvacite 2550, and N-methyl-2-pyrrolidone is added as a solvent. For device C, the intermediate structure consists only of Sylgard 184 on a glass slide, and a graphite gate is added to the heterostructure.

Data availability

The data that support the findings of this study are available at https://doi.org/10.5281/zenodo.5722484.

- Zhang, Y. et al. Giant phonon-induced conductance in scanning tunnelling spectroscopy of gate-tunable graphene. Nat. Phys. 4, 627–630 (2008).
- Hapala, P. et al. Mechanism of high-resolution STM/AFM imaging with functionalized tips Phys. Rev. B 90. 085421 (2014).
- Stroscio, J. A. & Celotta, R. J. Controlling the dynamics of a single atom in lateral atom manipulation. Science 306, 242–247 (2004).
- Wolter, B. et al. Spin friction observed on the atomic scale. Phys. Rev. Lett. 109, 116102 (2012).
- Daghero, D. & Gonnelli, R. S. Probing multiband superconductivity by point-contact spectroscopy. Supercond. Sci. Technol. 23, 043001 (2010).
- Kim, K. et al. Van der Waals heterostructures with high accuracy rotational alignment. Nano Lett. 16, 1989–1995 (2016).

Acknowledgements We thank P. Jarillo-Herrero, A. H. MacDonald and S. A. Kivelson for helpful discussions. We thank C.-L. Chiu, G. Farahi and H. Ding for helpful technical discussions. This work was primarily supported by the Gordon and Betty Moore Foundation's EPiQS initiative grant GBMF9469 and DOE-BES grant DE-FGO2-O7ER46419 to A.Y. Other support for the experimental work was provided by NSF-MRSEC through the Princeton Center for Complex Materials NSF-DMR-2011750 and NSF-DMR-1904442, ExxonMobil through the Andlinger Center for Energy and the Environment at Princeton, and the Princeton Catalysis Initiative. A.Y. acknowledges the hospitality of the Aspen Center for Physics, which is supported by the National Science Foundation grant PHY-1607611, and Trinity College, Cambridge, UK, where part of this work was carried out with the support of, in part, a QuantEmX grant from ICAM and the Gordon and Betty Moore Foundation through the grant GBMF9616. K.W. and T.T. acknowledge support from the Elemental Strategy Initiative conducted by the MEXT, Japan, grant JPMXP0112101001, and JSPS KAKENHI grants 19H05790 and JP20H00354.

Author contributions M.O., K.P.N., D.W. and A.Y. designed the experiment. M.O., D.W. and K.P.N. fabricated the devices used for the study. M.O., K.P.N., D.W. and R.L.L. carried out STM/STS and PCS measurements, with invaluable input from X.L. on the latter. M.O., D.W. and K.P.N. performed the data analysis. K.W. and T.T. synthesized the hBN crystals. All authors discussed the results and contributed to the writing of the manuscript.

Competing interests The authors declare no competing interests.

Additional information

 $\textbf{Supplementary information} \ The online version contains supplementary material available at https://doi.org/10.1038/s41586-021-04121-x.$

Correspondence and requests for materials should be addressed to Ali Yazdani.

Peer review information *Nature* thanks Dante Kennes and the other, anonymous, reviewer(s) for their contribution to the peer review of this work.

Reprints and permissions information is available at http://www.nature.com/reprints.